Research Article Vol. 4, No. 12 / December 2017 / Optica 1552

General-purpose, wide field-of-view reflection imaging with a tabletop 13 nm light source

Christina L. Porter,[1,5,†] Michael Tanksalvala,[1,4,†] Michael Gerrity,[1] Galen Miley,[2] Xiaoshi Zhang,[3] Charles Bevis,[1] Elisabeth Shanblatt,[1] Robert Karl, Jr.,[1] Margaret M. Murnane,[1,3] Daniel E. Adams,[1] and Henry C. Kapteyn[1,3]

[1]JILA, University of Colorado, Boulder, Colorado 80309-0440, USA
[2]Department of Chemistry, Northwestern University, 2145 Sheridan Road, Evanston, Illinois 60208, USA
[3]KMLabs Inc., 4775 Walnut St #102, Boulder, Colorado 80301, USA
[4]e-mail: michael.tanksalvala@colorado.edu
[5]e-mail: christina.porter@colorado.edu

Received 11 September 2017; revised 26 November 2017; accepted 27 November 2017 (Doc. ID 306738); published 20 December 2017

Lensless imaging with short-wavelength light is a promising method for achieving high-resolution, chemically sensitive images of a wide variety of samples. The use of 13 nm illumination is of particular interest for materials science and the imaging of next-generation nanofabricated devices. Prior to this work, there was an unmet need for a microscope that can image general samples with extreme ultraviolet light, which requires a reflection geometry. Here, we fulfill this need by performing lensless imaging using a 13 nm high-harmonic beam at grazing incidence, where most materials are reflective. Furthermore, we demonstrate to our knowledge the first 13 nm reflection-mode lensless microscope on a tabletop by using a compact high-harmonic generation source. Additionally, we present an analytic formalism that predicts when general lensless imaging geometries will yield Nyquist sampled data. Our grazing-incidence ptychographic approach, which we call GLIDER, provides the first route for achieving wide field-of-view, high-resolution, lensless images of general samples with extreme ultraviolet and soft x-ray light. © 2017 Optical Society of America under the terms of the OSA Open Access Publishing Agreement

OCIS codes: (100.5070) Phase retrieval; (110.1758) Computational imaging; (170.7440) X-ray imaging; (260.1960) Diffraction theory; (040.7480) X-rays, soft x-rays, extreme ultraviolet (EUV); (120.0120) Instrumentation, measurement, and metrology.

https://doi.org/10.1364/OPTICA.4.001552

1. INTRODUCTION

In recent years, extreme ultraviolet (EUV) and x-ray coherent diffraction imaging (CDI) [1,2], particularly using ptychography [3,4], has emerged as a robust method for imaging extended samples with high-contrast, diffraction-limited spatial resolution and chemical sensitivity [5–9]. However, most imaging with these wavelengths has been performed in a transmission geometry [10–13], which requires relatively thin samples (<1 μm). Imaging in reflection with this wavelength range has been less explored due to the low EUV/soft x-ray reflectivity of most samples near normal incidence, and the reconstruction challenges that arise from reflection geometries. A few notable reflection-mode experiments have been performed, allowing imaging at or near the surface of arbitrarily thick samples. These experiments have been performed both at synchrotrons [14–17] and using tabletop high-harmonic generation sources [5,18–20].

Near-normal-incidence, 13 nm reflection-mode CDI microscopes [15–17] have been implemented at synchrotron sources for imaging lithography masks. This geometry is effective for this application because masks are printed on multilayer mirrors designed for high reflectivity of 13 nm light. However, near normal incidence, general samples (i.e., those not fabricated on a multilayer mirror) typically cannot be imaged because of their low reflectivity (typically 0.001%–0.1% [21]). A grazing incidence was used in Ref. [14], utilizing a hard x-ray synchrotron source. However, this experimental geometry was sample-specific and not suitable for imaging general specimens since single-diffraction-pattern CDI was used, necessitating an isolated object.

Here we demonstrate the first general CDI microscope, to our knowledge, at the technologically important 13 nm wavelength by imaging at grazing incidence where most materials are reflective. This work also represents to our knowledge the first reflection-mode 13 nm lensless imaging performed at the tabletop scale. Furthermore, we develop the first straightforward, analytic approach to predict when off-axis or high-NA lensless imaging experiments will be properly sampled, which will be of use to the general lensless imaging community. We show, somewhat unexpectedly, that this grazing imaging mode allows us to combine a very wide field of view with high spatial resolution in ptychographic imaging.

The grazing-incidence geometry allows nearly any material to be imaged within reasonable exposure times using the photon flux

generated using a tabletop-scale 13 nm high-harmonic generation (HHG) light source. Materials generally have significant reflectivity (>1%) to 13 nm light at grazing incidence, and exhibit excellent chemical-specific contrast [21]. We call our technique GLancing Incidence Diffractive Imaging with EUV in Reflection, or GLIDER.

Most microscopes suffer from a fundamental tradeoff between field of view (FOV) and either resolution or data-acquisition time. In GLIDER, this tradeoff may be partially circumvented by exploiting the wide projected beam and conical diffraction that occurs on a sample at grazing incidence [14,22]. Without changing the sample-to-camera distance, the resolution in the direction of tilted incidence is decreased, but the resolution in the perpendicular direction is essentially unaffected. This yields significantly wider FOV images as compared to normal-incidence ptychography CDI for the same scan time. Contrastingly, in most conventional imaging modalities, obtaining a wider FOV in a set time period requires sacrificing resolution in all directions. Furthermore, simply tilting the sample in most imaging systems defocuses much of the FOV, negating the benefit of a wider projected beam. This typically forces a relaxed NA to increase the depth of focus, resulting in decreased resolution in all directions.

In GLIDER, the entire FOV remains in focus when the sample tilts, giving the full benefit of FOV extension. We believe this technique has wide applicability, especially for imaging semiconductor samples—in particular, grating-type structures including FINFET, memory, or overlay reference patterns that require large FOVs with directional high resolution.

2. SPATIALLY DEPENDENT OVERSAMPLING

In CDI, the oversampling constraint requires that the diffraction pattern (proportional to field intensity) must at least be Nyquist sampled by the detector in order to be reconstructed in a straightforward manner [1,23]. In ptychography, this limits the maximum allowable beam size on the sample for a given sample-to-camera distance and camera pixel size. At low numerical aperture (NA) and normal incidence, this requirement is given by

$$\sigma = \frac{\lambda z}{pD} \geq 2, \tag{1}$$

where λ is the wavelength, z is the sample-to-camera distance, p is the detector pixel size, D is the diameter of the beam, and σ is the oversampling, which must be greater than 2 to ensure Nyquist sampled data. At high NA or non-normal incidence, Eq. (1) ceases to hold because conical diffraction from the sample changes the spacing between diffracted orders from that predicted using a Fourier transform relationship between the sample and detector planes [see Fig. 1(b)]. This results in spatially dependent oversampling on the detector.

When a round beam of diameter D [Fig. 1(b), left] is incident on a sample at grazing incidence, the projection of the beam in the sample plane becomes wide [Fig. 1(b), center], stretching the beam to a diameter of $D/\sin(\alpha)$, where α is the incidence angle between the sample surface and the beam. Using parameters relevant to the present experiment and Eq. (1), at normal incidence we would predict an oversampling of 6.8 in the horizontal direction. For the same beam at grazing incidence with a projected width of 70.1 μm, Eq. (1) would predict an oversampling of 1.1, suggesting that the data would not be Nyquist sampled on the detector and thus would not reconstruct [1] without advanced techniques such as [24,25] that require smaller scan steps and thus increased data-acquisition time. However, if we take into account the spatially dependent oversampling due to conical diffraction in this grazing-incidence geometry, we predict a minimum oversampling of 3.6 and max oversampling of 12.4 on the detector [see Fig. 2(f)], suggesting that the data actually

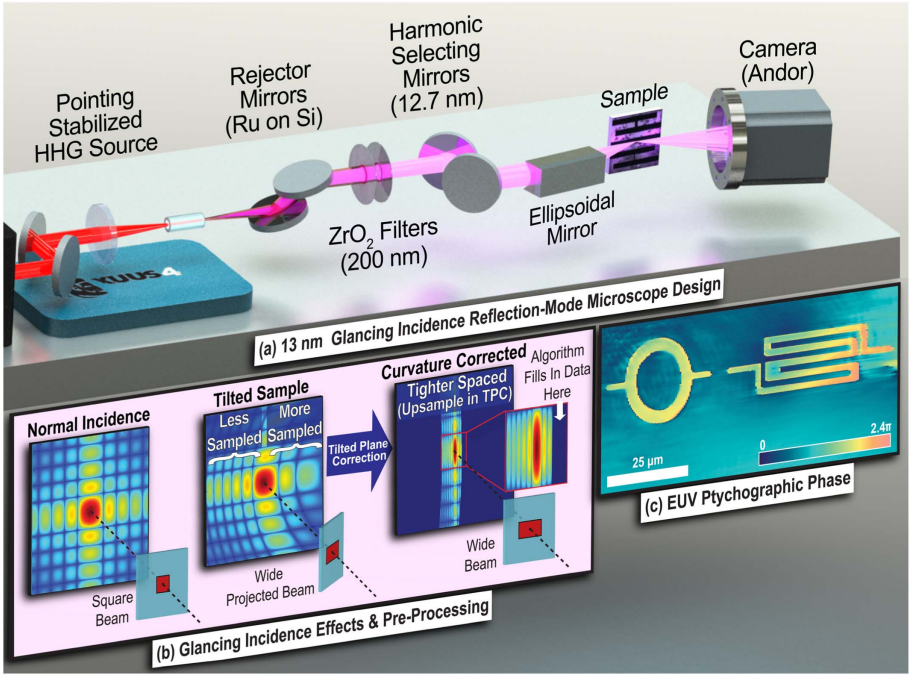

Fig. 1. (a) 13 nm reflection-mode lensless microscope design (GLIDER). (b) Comparison of diffraction patterns due to a small square beam at normal incidence (left), the resulting wide projected beam due to tilting the sample (middle), and the post-TPC diffraction (right) identical to diffraction due to a wide beam at normal incidence. (c) 13 nm ptychographic unwrapped phase reconstruction.

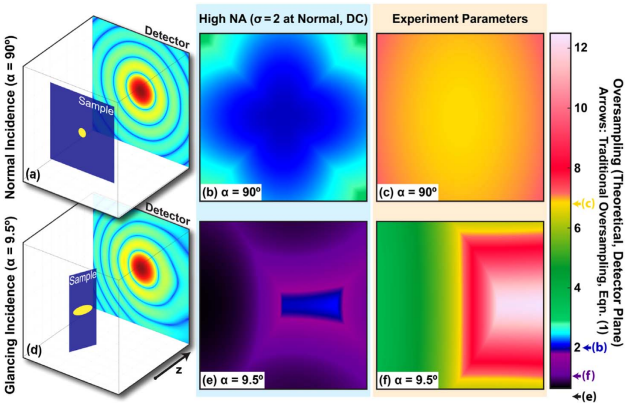

Fig. 2. Results of new analytic spatially dependent oversampling formalism. Representative diffraction patterns (logarithmic colorscale) from (a) a round beam at normal incidence versus (d) grazing incidence. In (b) and (e), the theoretical spatially dependent oversampling on a 2048 × 2048 pixel camera with 13.5 μm square pixels is shown for a high-NA geometry with a round beam, where $\sigma = 2$ according to Eq. (1). Spatially dependent oversampling is compared for (b) normal incidence versus (e) grazing incidence. In (c) and (f), the theoretical oversampling is shown on the same detector for the experimental geometry used in this work ($z = 84.4$ mm, beam with height 6.5 μm and width 11.6 μm at normal incidence). Images (b) and (c) are at normal incidence; (e) and (f) are at grazing incidence ($\alpha = 9.5°$). The oversampling predicted by Eq. (1) for the geometries in (b), (c), (e), and (f) is shown on the colorbar. See Visualization 1.

can be reconstructed even in the presence of a wide projected beam that would apparently violate Eq. (1).

We derive the spatially dependent oversampling at high NA and tilted incidence, and present numeric simulations to confirm it in Supplement 1. Our derivation is based upon analytically propagating pairs of Dirac delta functions that trace out the shape of the beam in the sample plane to the detector plane using the Rayleigh–Sommerfeld formalism [26]. In the detector plane, the resulting highest frequencies observed are compared to the pixel spacing in the direction these frequencies occur, on a pixel-by-pixel basis. Figure 2 shows representative diffraction patterns at normal (a) versus grazing (d) incidence for a round beam. In Fig. 2(b), the theoretical spatially dependent oversampling at normal incidence for a round beam oversampled by 2 according to Eq. (1) at the DC (center pixel) is shown for a detector with 2048 × 2048 pixels that are 13.5 μm square. The oversampling for the same detector and beam geometry is shown in Fig. 2(e) at a grazing incidence of 9.5° from the sample surface. The same normal/grazing incidence comparison is shown in Figs. 2(c) and 2(f) for the experimental geometry used here (84.4 mm between sample and camera, 6.5 × 11.6 μm beam at normal incidence).

3. EXPERIMENT

Our GLIDER microscope [see Fig. 1(a)] uses an ultrafast Ti:Sapphire oscillator-amplifier system at 795 nm (KMLabs Wyvern-HP). The 3 mJ, 38 fs pulses at 3 kHz drive a 13 nm HHG source (KMLabs XUUS 4.0). High-harmonic generation of coherent 13 nm light occurs in a 150 μm inner diameter, hollow glass waveguide filled with 700 Torr He gas, into which the pointing-stabilized IR laser light is focused. After the waveguide, residual fundamental laser light co-propagating with the emitted EUV beam is removed using two rejecter mirrors oriented near Brewster's angle for the 795 nm light, as well as two 200 nm thick ZrO_2 filters. Next, the 12.6 nm harmonic is selected using two 45° angle of incidence multilayer Mo:Si mirrors. The EUV beam is then focused onto the sample using an ellipsoidal focusing optic to a spot size of ~6.5 × 11.6 μm ($1/e^2$ diameter, as viewed at normal incidence). The sample is placed at a grazing incidence to the beam, with an angle of 9.5° between the sample surface and the incident beam. At this incidence angle, the projected beam's $1/e^2$ diameter becomes 6.5 × 70.1 μm wide. The sample consisted of 29-nm-tall nickel structures deposited on a Si wafer. The sample was scanned using a Fermat spiral pattern [27] with nominally 1.56 μm between each of 121 adjacent scan positions. Diffraction patterns were detected on a 2048 × 2048 Andor iKon-L CCD detector with 13.5 μm pixels, 84.4 mm from the sample.

4. RESULTS

A reconstructed image using 13 nm GLIDER is shown in Fig. 3. The full FOV object intensity [Fig. 3(a)] is compared to a scanning electron microscopy (SEM) image of the same region [Fig. 3(b)]. The substrate discoloration in the center of both images is due to contamination buildup from extensive prior imaging performed on this sample using a 30 nm EUV microscope. The square discoloration in Fig. 3(b) is due to hydrocarbon buildup from a few prior SEM images of the sample. We see good agreement between the ptychographic intensity, phase images, and the SEM in both the narrow [Figs. 3(c) and 3(d)] and full fields of view.

Prior to performing ptychographic reconstructions, the data was remapped onto a linear frequency grid using tilted-plane correction (TPC) [14,22], allowing the fast Fourier transform to be used during reconstructions even though the raw data shows extreme conical diffraction [see Fig. 1(b)]. To ensure that originally oversampled data remained so after the remapping, the diffraction patterns were interpolated during TPC onto a grid with eight times finer spacing in the horizontal direction and two times finer spacing in the vertical direction compared to the detector grid. This upsampling step is crucial to GLIDER because, if not performed, all of the data will be remapped during TPC to the oversampling predicted by Eq. (1) ($\sigma = 1.1$), which is lower than the detector's oversampling at *any* pixel ($\sigma_{\min} = 3.6$).

Ptychographic reconstructions were performed using a combination of the extended and regularized ptychographic iterative engines (ePIE [4] and rPIE [28]). We found that running ePIE (equivalent to rPIE with $\alpha = 1$) to solve for the probe and rPIE (with $\alpha = 0.5$) as a refinement gave better results than starting with rPIE, which was prone to yielding multiple copies of the probe on the large probe grid resulting from upsampling in TPC. We note that this work is the first to apply rPIE to experimental data. We also used the Shrinkwrap algorithm [29] to constrain the probe; its first application in this capacity in ptychography to our knowledge. By running Shrinkwrap on the probe for just a few iterations relatively early in the reconstruction, we were able to suppress the development of artifacts in the reconstructed beam without having to carefully tune the Shrinkwrap parameters. More details about the reconstruction process are given in Supplement 1.

During all iterations, we added a saturation constraint to our ptychographic algorithm. We set pixels whose reconstructed reflectivity was brighter than a reasonable maximum (which is typically 1 in quantitative reconstructions as in Ref. [5]) back

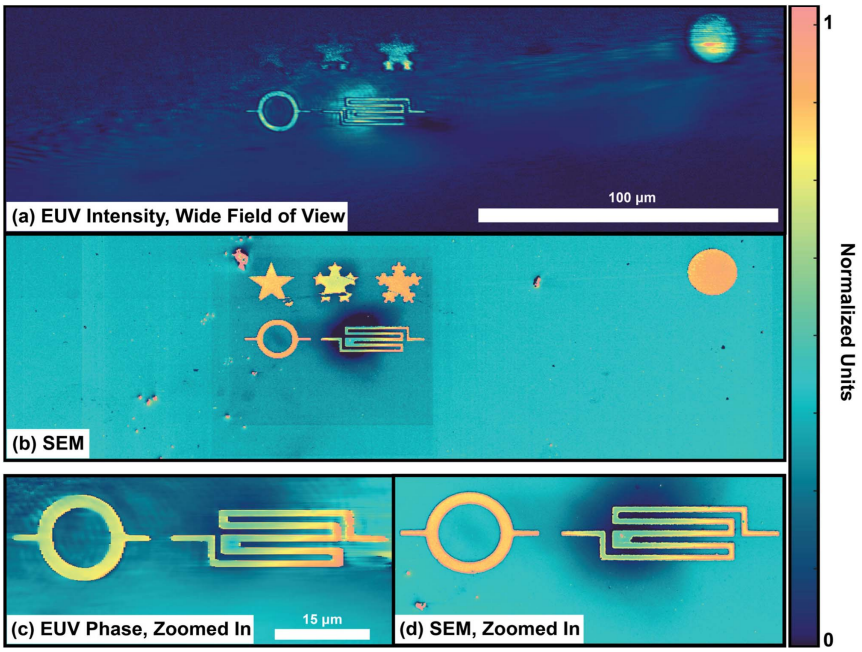

Fig. 3. (a) EUV ptychography intensity image, full field of view. (b) SEM with rectangular darkening due to hydrocarbon burn-on from prior SEM imaging completed after the EUV ptychography data was obtained. (c) EUV ptychography unwrapped phase image, zoomed in to reveal detail. (d) SEM image, zoomed in to reveal detail. Images (a) and (b) share a scale bar, as do images (c) and (d); all share the colorbar. Note that the roughly round discoloration visible in all of these images on the left side of the labyrinth-like structure and on the substrate beneath it is due to hydrocarbon deposition. This deposition resulted from extensive previous imaging experiments on this sample using a different EUV microscope that illuminated the sample in these regions with focused illumination.

to that threshold value. This helped prevent the ptychographic algorithm from reconstructing copies of the probe at the edges of the large grid and made the reconstructions significantly more stable. Because we had uncertainty in the beam power, we set a looser threshold (eight times the average sample reflectivity).

Due to the asymmetry arising from conical diffraction, the detector collected higher spatial frequency information on one side of the detector than the other. We reconstructed to an NA of 0.0075, at which point there was missing data on the right hand (lower NA) side of the detector starting at an NA of 0.003. We allowed the ptychographic algorithm to fill in this missing data using a method similar to super-resolution ptychography [13,30]. We note that this is an easier problem to solve than the case of super-resolution (which uses extrapolation) because there *is* some information at the desired high spatial frequencies present on the detector. Furthermore, we constrained the maximum allowable intensity in the unmeasured parts of Fourier space—where the algorithm was allowed to fill in data—not to exceed that of the nearest known pixels. This is equivalent to setting a lower saturation constraint threshold in the "super-resolution" region on the detector [i.e., the region indicated by the white arrow in the inset on the right side of Fig. 1(b)].

5. DISCUSSION

Figure 4(a) is a 1.2 megapixel image with a >250 μm wide FOV. The overlaid lines on this reconstruction delimit the maximum extent of the scan positions (magenta), the beam intensity's $1/e^2$ diameter (orange), and its $1/e^4$ diameter (white). Figure 4(b) shows the wide reconstructed beam intensity.

The 121-position Fermat spiral horizontally spans only 26% of the beam's $1/e^2$ width, and subtends an area of only 290 μm^2 (shown in magenta in Fig. 4). In comparison, the well-reconstructed area shown in Fig. 3(c) is 1630 μm^2, a 5.6 times larger area than the beam's center was scanned over. Good image fidelity extends throughout the region illuminated by the $1/e^2$ intensity of the beam during the scan [shown in cyan in Fig. 4(a)] totaling 2370 μm^2, 8.2 times larger than the scan area. Impressively, regions within the beam's full $1/e^4$ extent (>9810 μm^2, 34 times the scan area, shown in white) reconstruct with somewhat lower image fidelity. Recognizably correct structures, such as the stars and filled-in circle, extend even outside of this region.

Because we had not yet developed the spatially dependent oversampling formalism at the time of data acquisition, we could not predict whether or not our data would be oversampled. Thus, we used scan steps that were small enough to obtain convergence using reconstruction algorithms that can handle somewhat undersampled data [24,25]. After developing the sampling formalism presented here and finding that traditional ptychography actually could be used to reconstruct this data, it became clear that our step sizes could have been the typical size for ptychography (1/2 of the beam radius on the sample [4]) because we did not have to correct for undersampled data on our detector. Had we used that larger step size, then the beam center would have been scanned over a full 350 μm in the horizontal direction, increasing our reconstructed FOV to over 0.6 mm wide for the same data-acquisition time. The well-reconstructed area would have more than quadrupled, with good image fidelity over 10,500 μm^2 and recognizable features beyond 20,000 μm^2. Furthermore,

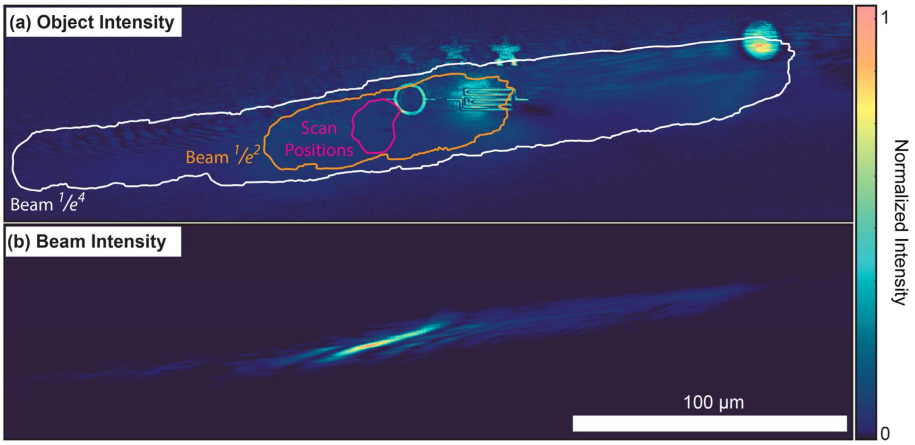

Fig. 4. (a) GLIDER intensity image overlaid with the maximum extent during the scan of the beam's center (magenta), its $1/e^2$ diameter (orange), and its $1/e^4$ diameter (white). (b) Reconstructed beam intensity. Scale bar and colorbar are shared. Note that, in the experiment, the beam was horizontal and the sample was tilted.

scanning the beam center over a full beam width would likely have led to more robust convergence for a wider set of input parameters in ptychography. The convergence we obtained in spite of the small scan size shows potential for use in systems where physical constraints limit the sample's travel range.

The reconstructed images in Figs. 3(a), 3(c), and 4 have a pixel size of 77.5 nm (tall) by 265 nm (wide). This resolution discrepancy between the horizontal and vertical directions is a result both of the stretching induced by conical diffraction and the cropping of the diffraction pattern more in the horizontal than vertical direction after TPC due to the diffracted DC peak being off-center on our camera and a limited signal-to-noise ratio for this sample. In theory, for a high-SNR dataset with a well-centered DC peak, the resolution for this experimental geometry could have been 40 nm in the vertical direction and 160 nm in the horizontal, so long as the asymmetrically missing data on the well-oversampled side of the detector were accurately filled in by super-resolution ptychography. Had we instead used a normal-incidence geometry with a wide beam (increasing z to 269 mm to maintain $\sigma > 3.6$), we would have seen the typical FOV/resolution tradeoff, with 123 nm pixels in both directions. Using GLIDER, we decouple the horizontal direction's FOV/resolution tradeoff from that of the vertical, enabling high-directional-resolution, wide-FOV imaging.

6. CONCLUSION

We have demonstrated the first 13 nm lensless imaging, to our knowledge, on a tabletop in a reflection geometry. Our grazing-incidence GLIDER microscope is the first general 13 nm microscope using *any* source capable of imaging extended, thick samples with a wide variety of compositions. This generality is due to the high reflectivity of most materials at grazing incidence.

By using a grazing-incidence geometry, we obtain extremely wide FOV images with GLIDER. In doing so, we sacrifice some resolution in the direction in which we tilt the sample, while retaining the high resolution that we would have had with a round beam at normal incidence in the perpendicular direction. Thus, to obtain a large FOV, we lose resolution in only one instead of both directions, as is the case in most imaging modalities.

We have derived the spatially dependent oversampling on the detector that arises in grazing incidence and high-NA geometries. We have also described the necessary upsampling during the tilted plane correction pre-processing step to achieve properly sampled data that can be reconstructed with traditional ptychographic or other CDI algorithms. We have furthermore discussed reconstruction techniques that help yield stable reconstructions when a very large probe grid is used.

We believe the GLIDER technique using 13 nm and shorter wavelengths will find broad applicability in materials and device science. It is extremely well suited for nanoelectronic device inspection where a wide FOV and directional high resolution is necessary, such as imaging gratings, metamaterials, and next-generation semiconductor devices.

Funding. National Science Foundation (NSF) (DMR-1548924, 1144083); Gordon and Betty Moore Foundation (EPiQS Initiative Grant GMBF); Katharine Burr Blodgett Fellowship; Defense Advanced Research Projects Agency (DARPA) (W31P4Q-13-1-0015); U.S. Department of Defense (DOD) (NDSEG fellowship).

See Supplement 1 for supporting content.

†These authors contributed equally to this work.

REFERENCES

1. D. Sayre, "Some implications of a theorem due to Shannon," Acta Crystallogr. **5**, 843 (1952).
2. J. R. Fienup, "Phase retrieval algorithms: a comparison," Appl. Opt. **21**, 2758–2769 (1982).
3. J. M. Rodenburg and H. M. L. Faulkner, "A phase retrieval algorithm for shifting illumination," Appl. Phys. Lett. **85**, 4795–4797 (2004).
4. A. M. Maiden and J. M. Rodenburg, "An improved ptychographical phase retrieval algorithm for diffractive imaging," Ultramicroscopy **109**, 1256–1262 (2009).
5. E. R. Shanblatt, C. L. Porter, D. F. Gardner, G. F. Mancini, R. M. Karl, M. D. Tanksalvala, C. S. Bevis, V. H. Vartanian, H. C. Kapteyn, D. E. Adams, and M. M. Murnane, "Quantitative chemically specific coherent diffractive imaging of reactions at buried interfaces with few nanometer precision," Nano Lett. **16**, 5444–5450 (2016).

6. H. N. Chapman, A. Barty, M. J. Bogan, S. Boutet, M. Frank, S. P. Hau-Riege, S. Marchesini, B. W. Woods, S. Bajt, W. H. Benner, R. A. London, E. Plönjes, M. Kuhlmann, R. Treusch, S. Düsterer, T. Tschentscher, J. R. Schneider, E. Spiller, T. Möller, C. Bostedt, M. Hoener, D. A. Shapiro, K. O. Hodgson, D. van der Spoel, F. Burmeister, M. Bergh, C. Caleman, G. Huldt, M. M. Seibert, F. R. N. C. Maia, R. W. Lee, A. Szöke, N. Timneanu, and J. Hajdu, "Femtosecond diffractive imaging with a soft-x-ray free-electron laser," Nat. Phys. **2**, 839–843 (2006).
7. R. L. Sandberg, A. Paul, D. A. Raymondson, S. Hadrich, D. M. Gaudiosi, J. Holtsnider, R. I. Tobey, O. Cohen, M. M. Murnane, and H. C. Kapteyn, "Lensless diffractive imaging using tabletop coherent high-harmonic soft-x-ray beams," Phys. Rev. Lett. **99**, 098103 (2007).
8. J. Miao, P. Charalambous, J. Kirz, and D. Sayre, "Extending the methodology of x-ray crystallography to allow imaging of micrometre-sized non-crystalline specimens," Nature **400**, 342–344 (1999).
9. J. Miao, T. Ishikawa, I. K. Robinson, and M. M. Murnane, "Beyond crystallography: diffractive imaging using coherent x-ray light sources," Science **348**, 530–535 (2015).
10. B. Zhang, M. D. Seaberg, D. E. Adams, F. Dennis, E. R. Shanblatt, J. M. Shaw, W. Chao, E. M. Gullikson, F. Salmassi, H. C. Kapteyn, and M. M. Murnane, "Full field tabletop EUV coherent diffractive imaging in a transmission geometry," Opt. Express **21**, 21970–21980 (2013).
11. D. F. Gardner, M. Tanksalvala, E. R. Shanblatt, X. Zhang, B. R. Galloway, C. L. Porter, R. Karl Jr., C. Bevis, D. E. Adams, H. C. Kapteyn, M. M. Murnane, and G. F. Mancini, "Subwavelength coherent imaging of periodic samples using a 13.5 nm tabletop high-harmonic light source," Nat. Photonics **11**, 259–263 (2017).
12. M. Holler, M. Guizar-Sicairos, E. H. Tsai, R. Dinapoli, E. Muller, O. Bunk, J. Raabe, and G. Aeppli, "High-resolution non-destructive three-dimensional imaging of integrated circuits," Nature **543**, 402–406 (2017).
13. K. Giewekemeyer, P. Thibault, S. Kalbfleisch, A. Beerlink, C. M. Kewish, M. Dierolf, F. Pfeiffer, and T. Salditt, "Quantitative biological imaging by ptychographic x-ray diffraction microscopy," Proc. Natl. Acad. Sci. U.S.A. **107**, 529–534 (2010).
14. T. Sun, Z. Jiang, J. Strzalka, L. Ocola, and J. Wang, "Three-dimensional coherent x-ray surface scattering imaging near total external reflection," Nat. Photonics **6**, 588–592 (2012).
15. P. Helfenstein, I. Mohacsi, R. Rajeev, and Y. Ekinci, "Scanning coherent diffractive imaging methods for actinic EUV mask metrology," J. Micro/Nanolithogr. MEMS MOEMS **15**, 034006 (2016).
16. T. Harada, H. Hashimoto, T. Amano, H. Kinoshita, and T. Watanabe, "Actual defect observation results of an extreme-ultraviolet blank mask by coherent diffraction imaging," Appl. Phys. Express **9**, 035202 (2016).
17. I. Mochi, P. Helfenstein, I. Mohacsi, R. Rajendran, S. Yoshitake, and Y. Ekinci, "RESCAN: an actinic lensless microscope for defect inspection of EUV reticles," Proc. SPIE **10143**, 101431O (2017).
18. M. Zürch, C. Kern, and C. Spielmann, "XUV coherent diffraction imaging in reflection geometry with low numerical aperture," Opt. Express **21**, 21131–21147 (2013).
19. M. D. Seaberg, B. Zhang, D. F. Gardner, E. R. Shanblatt, M. M. Murnane, H. C. Kapteyn, and D. E. Adams, "Tabletop nanometer extreme ultraviolet imaging in an extended reflection mode using coherent Fresnel ptychography," Optica **1**, 39–44 (2014).
20. B. Zhang, D. F. Gardner, M. H. Seaberg, E. R. Shanblatt, C. L. Porter, R. Karl, C. A. Mancuso, H. C. Kapteyn, M. M. Murnane, and D. E. Adams, "Ptychographic hyperspectral spectromicroscopy with an extreme ultraviolet high harmonic comb," Opt. Express **24**, 18745–18754 (2016).
21. B. L. Henke, E. M. Gullikson, and J. C. Davis, "X-ray interactions: photoabsorption, scattering, transmission, and reflection at E = 50-30,000 eV, Z = 1-92," At. Data Nucl. Data Tables **54**, 181–342 (1993).
22. D. F. Gardner, B. Zhang, M. D. Seaberg, L. S. Martin, D. E. Adams, F. Salmassi, E. Gullikson, H. Kapteyn, and M. Murnane, "High numerical aperture reflection mode coherent diffraction microscopy using off-axis apertured illumination," Opt. Express **20**, 19050–19059 (2012).
23. C. E. Shannon, "Communication in the presence of noise," Proc. IRE **37**, 10–21 (1949).
24. T. B. Edo, D. J. Batey, A. M. Maiden, C. Rau, U. Wagner, Z. D. Pešić, T. A. Waigh, and J. M. Rodenburg, "Sampling in x-ray ptychography," Phys. Rev. A **87**, 053850 (2013).
25. D. J. Batey, T. B. Edo, C. Rau, U. Wagner, Z. D. Pešić, T. A. Waigh, and J. M. Rodenburg, "Reciprocal-space up-sampling from real-space oversampling in x-ray ptychography," Phys. Rev. A **89**, 043812 (2014).
26. J. W. Goodman, *Introduction to Fourier Optics*, 3rd ed. (Roberts, 2005).
27. X. Huang, H. Yan, R. Harder, Y. Hwu, I. K. Robinson, and Y. S. Chu, "Optimization of overlap uniformness for ptychography," Opt. Express **22**, 12634–12644 (2014).
28. A. Maiden, D. Johnson, and P. Li, "Further improvements to the ptychographical iterative engine," Optica **4**, 736–745 (2017).
29. S. Marchesini, H. He, H. N. Chapman, S. P. Hau-Riege, A. Noy, M. R. Howells, U. Weierstall, and J. C. H. Spence, "X-ray image reconstruction from a diffraction pattern alone," Phys. Rev. B **68**, 140101 (2003).
30. A. M. Maiden, M. J. Humphry, F. Zhang, and J. M. Rodenburg, "Superresolution imaging via ptychography," J. Opt. Soc. Am. A **28**, 604–612 (2011).

128.138.140.254 {ts '2018-01-25 12:44:59'}